Bulletin of the Seismological Society of America, Vol. 96, No. 5, pp. 1764–1778, October 2006, doi: 10.1785/0120060024

Comparison of Fault Representation Methods in Finite Difference Simulations of Dynamic Rupture

by Luis A. Dalguer and Steven M. Day

Abstract Assessing accuracy of numerical methods for spontaneous rupture simulation is challenging because we lack analytical solutions for reference. Previous comparison of a boundary integral method (BI) and finite-difference method (called DFM) that explicitly incorporates the fault discontinuity at velocity nodes (traction-at-split-node scheme) shows that both converge to a common, grid-independent solution and exhibit nearly identical power-law convergence rates with respect to grid spacing Δx. We use this solution as a reference for assessing two other proposed finite-difference methods, the thick fault (TF) and stress glut (SG) methods, both of which approximate the fault-jump conditions through inelastic increments to the stress components (inelastic-zone schemes). The TF solution fails to match the qualitative rupture behavior of the reference solution and has quantitative misfits in root-mean-square rupture time of ~30% for the smallest computationally feasible Δx (with ~9 grid-point resolution of cohesive zone, denoted $\overline{N}_c = 9$). For sufficiently small values of Δx, the SG method reproduces the qualitative features of the reference solution, but rupture velocity remains systematically low for SG relative to the reference solution, and SG lacks the well-defined power-law convergence seen for BI and DFM. The rupture-time error for SG, with $\overline{N}_c \sim 9$, remains well above uncertainty in the reference solution, and the split-node method attains comparable accuracy with $\overline{N}_c$ 1/4 as large (and computation timescales as $(\overline{N}_c)^4$). Thus, accuracy is highly sensitive to the formulation of the fault-jump conditions: The split-node method attains power-law convergence. The SG inelastic-zone method achieves solutions that are qualitatively meaningful and quantitatively reliable to within a few percent, but convergence is uncertain, and SG is computationally inefficient relative to the split-node approach. The TF inelastic-zone method does not achieve qualitatively meaningful solutions to the 3D test problem and is sufficiently computationally inefficient that it is not feasible to explore convergence quantitatively.

Introduction

A physical understanding of the spontaneous rupture process is important for advancing our understanding of earthquake physics in general, and is an essential component of efforts to reduce uncertainties in numerical simulations of earthquake ground motion. Despite limitations, the idealized model of rupture as a dynamically running shear crack on a frictional interface embedded in a linearly elastic continuum has proven to be a useful foundation for analyzing natural earthquakes (e.g., Andrews, 1976a,b; Das and Aki, 1977; Day, 1982a,b; Olsen *et al.*, 1997) and their experimental analogues (e.g., Day and Ely, 2002; Xia *et al.*, 2005). This model leads to nonlinear, mixed boundary value problems. The nonlinearity occurs because the respective domains of the kinematic and dynamic boundary conditions are time dependent, and these domains have to be determined dynamically as part of the solution itself. The theoretical study of this problem class is usually possible only with computationally intensive numerical methods that solve the elastodynamic equations of motion in the continuum, coupling them to additional equations governing frictional sliding on the boundary representing the fault surface.

The challenges in validating the numerical methods are discussed in some detail by, e.g., Day and Ely (2002) and Day *et al.* (2005, hereafter D05). The fundamental problem is that there are no analytical solutions available to provide an absolute standard against which to validate numerical solutions to nonlinear 3D spontaneous rupture. Harris *et al.* (2004) defined a benchmark spontaneous rupture problem and proposed that numerical solutions to this problem, as obtained by independent methods, be compared with each other, as one means of assessing numerical accuracy of the methods. The Harris *et al.* benchmark is formulated for a

fault plane in a uniform, infinite, isotropic elastic space, and therefore can be solved by boundary-integral (BI) methods as well as by finite-difference (FD), finite-element, and other volume discretizaton methods.

D05 performed a detailed comparison of solutions to the Harris *et al.* benchmark as calculated, respectively, by a BI method and a so-called traction-at-split-node (TSN) FD method called DFM (Day, 1982b; Day and Ely, 2002). They argued that the BI method has a high degree of independence from volume-discretization methods such as DFM. In contrast to the latter, the BI method is semianalytical, in that it discretizes only the fault-surface points, representing the reaction of the continuum to slip at those points with an exact Green's function. As a consequence, the BI method is not subject to the numerical dispersion that is a dominant source of error in the volume-discretization methods. Given this independence of the methods, D05 proposed that the level of misfit between their BI and DFM solutions to the Harris *et al.* benchmark problem be used to estimate a bound on the error of both solutions. They found that the two methods converged, with decreasing spatial-discretization interval Δx, to a common solution, to within well-defined tolerances for three specific error metrics: the root mean square average of the differences of the rupture time, final slip, and peak value of slip velocity, respectively, between solutions.

This article assesses the accuracy of two additional FD methods that have been proposed for solving spontaneous rupture problems, the thick fault (TF) method proposed by Madariaga *et al.* (1998) and the so-called stress glut (SG) method first presented by Andrews (1976a) for modeling yielding off the fault, and subsequently described by Andrews (1999) for fault-rupture problems. The TF and SG methods differ from the DFM method, in that DFM explicitly incorporates a discontinuity at velocity nodes, whereas TF and SG do not. Instead, TF and SG represent the fault discontinuity through inelastic increments to stress components, and we therefore refer to them collectively as inelastic-zone methods. We perform the assessment of these FD methods by using them to compute solutions to the Harris *et al.* (2004) benchmark problem. Then, using the D05 numerical solution as a reference, we compute the three error metrics proposed in that study and examine their dependence on Δx. We find that, independently of the type of spatial differencing used in grid interior, the FD solution accuracy is very sensitive to the method used to represent the fault-plane discontinuity. The SG method converges relatively slowly (compared with BI and DFM) to the reference solution, and we are unable to achieve reasonable convergence with the TF method.

Description of Fault Models

Numerous formulations have been used to solve the spontaneous rupture problem by the FD method (e.g., Andrews, 1976a,b, 1999; Madariaga, 1976; Day 1982a,b; Madariaga *et al.*, 1998; Inoue and Miyatake, 1998; Cruz-Atienza and Virieux, 2004; Kase and Day, 2006), the finite-element (FE) method (e.g., Oglesby *et al.*, 1998, 2000; Aagaard *et al.*, 2001), and the BI method (e.g., Das, 1980; Andrews, 1985; Das and Kostrov, 1988; Fukuyama and Madariaga, 1998; Aochi and Fukuyama, 2002; Lapusta *et al.*, 2000). In addition, inherently discrete representations of the problem include the lattice models used by Mora and Place (1994) and Morgan (1999) and the discrete-element method (DEM) used by Dalguer *et al.* (2001, 2003).

In current practice, the fault representation favored in FD schemes seems to depend in part upon the numerical technique used for the discretization of the elastodynamic equations. Consider, for example, the fourth-order velocity-stress staggered-grid (VSSG) FD method for elastodynamics, introduced by Levander (1988), then elaborated, for example, by Graves (1996) for 3D applications and by Moczo *et al.* (2002) for application to heterogeneous media. The VSSG method is one of the most widely used methods for solving complex seismic-wave propagation problems. The methods that have so far been devised to adapt the VSSG method to spontaneous-rupture problems in general do not explicitly incorporate a fault discontinuity at velocity nodes. Rather, the fault discontinuity is represented through inelastic increments to stress components at a set of stress nodes taken to lie on the fault surface. With this type of discretization, the fault surface is indistinguishable from an inelastic zone with a thickness given by the spatial step Δx (or an integral multiple of Δx), and we therefore refer to these fault representations as inelastic-zone methods. In this article, we consider two well-known examples of this approach, the TF method proposed by Madariaga *et al.* (1998), and the SG method described by Andrews (1976a, 1999). A review of different approaches for modeling fault discontinuities in several classes of FD methods was recently presented by Moczo *et al.* (2006).

In contrast, other continuum discretizations lend themselves readily to an explicit incorporation of discontinuous velocity nodes, so-called split nodes. This approach seems to be favored in FD schemes that (1) employ second-order spatial differencing and (2) collocate all three velocity components at a common set of grid vertices, with all six stress components collocated at the corresponding cell centroids (e.g., Andrews, 1973, 1976a,b; Day, 1982a,b; D05). The split-node approach is prevalent in schemes meeting these criteria because these schemes permit a natural partition of the equations of motion into separate parts governing each side of the surface on which the split nodes lie (see, for example, D05, appendix A). That is, this partition is such that the only influence transmitted across this interface occurs through the tractions (frictional resistance and normal traction) acting at the interface itself. Andrews (1999) calls this fault treatment the TSN method. The same natural partitioning readily applies to FE methods, where the split-node approach has also found favor (e.g., Oglesby *et al.*, 1998; Aagaard *et al.*, 2001). In contrast, somewhat more substantial modification would be required to effect a similar par-

titioning of the fourth-order VSSG scheme, which probably accounts for the preference for inelastic-zone fault models for use with the VSSG scheme. On the other hand, we have shown (Dalguer and Day, 2006) that the split-node treatment can be easily applied to the VSSG scheme if the spatial differencing along the fault plane is reduced to second order.

Fault-Jump Conditions

We formulate the fault-surface jump conditions according to D05. We denote the shear-traction vector on the fault by $\boldsymbol{\tau}$, the tangential displacement discontinuity (slip) vector by $\mathbf{s}$, their respective magnitudes by τ and s, and the frictional shear strength by τ_c. To set the sign conventions, we note that $\boldsymbol{\tau} = (\mathbf{I} - \hat{\mathbf{n}}\hat{\mathbf{n}}) \cdot \boldsymbol{\sigma} \cdot \hat{\mathbf{n}}$, where $\boldsymbol{\sigma}$ is the stress tensor, $\mathbf{I}$ is the identity tensor, and $\hat{\mathbf{n}}$ is the unit normal to the fault. We define negative and positive sides of the fault surface such that $\hat{\mathbf{n}}$ is directed from the former toward the latter, and let $\mathbf{s}$ represent tangential displacement of the positive side relative to the negative side. The fault conditions are

$$\tau_c - \tau \geq 0, \tag{1}$$

$$\tau_c \dot{\mathbf{s}} - \boldsymbol{\tau} \dot{s} = 0. \tag{2}$$

Equation (1) then stipulates that the shear traction be bounded by the (current value of) frictional strength, and equation (2) stipulates that any nonzero velocity discontinuity be opposed by an antiparallel traction (i.e., the negative side exerts traction $-\boldsymbol{\tau}$ on the positive side) with magnitude equal to the frictional strength τ_c. The frictional strength evolves according to some specified friction law and may depend on normal stress, slip, slip velocity, and other mechanical or thermal variables.

TSN Formulation

The TSN boundary formulation was reviewed by Andrews (1999), and the details of our implementation in the DFM code have been described in D05. Here we give only a brief summary of the method, following the notation of D05.

We position the fault on the $x - y$ plane. As shown in Figure 1, a given fault-plane node is split into plus-side and minus-side parts, with respective lumped nodal masses M^+ and M^-. The separate contributions from each side of the fault due to deformation of neighboring elements produce elastic restoring forces (nodal forces), R^+ and R^-. At a particular time (t), D'Alembert's principle leads to a nodal equilibrium equation of motion for each split node. At each step of integration the equation is solved by the central FD scheme to estimate the vector components of velocity ($\dot{u}_v^{\pm}$) and displacement ($u_v^{\pm}$) at a given node,

$$\begin{aligned} \dot{u}_v^{\pm}(t + \Delta t/2) &= \dot{u}_v^{\pm}(t - \Delta t/2) + \Delta t (M^{\pm})^{-1} \\ &\quad \{R_v^{\pm}(t) \mp a[T_v(t) - T_v^0]\} \\ u_v^{\pm}(t + \Delta t) &= u_v^{\pm}(t) + \Delta t \dot{u}_v^{\pm}(t + \Delta t/2), \end{aligned} \tag{3}$$

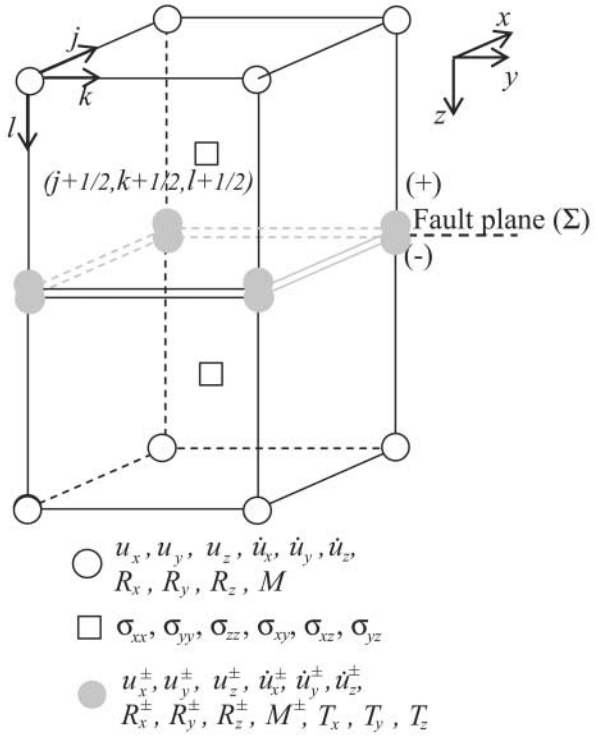

Figure 1. Split-node geometry of DFM, illustrated for two cubic unit cells. Mass is split, and separate elastic-restoring forces (nodal forces) act on the two halves. The two halves of a split node interact only through shear and normal tractions at the interface.

where v indicates the vector components (x or y) tangential to the fault, Δt is the time step, a is the area of the fault surface associated with each split node, T_v is the nodal value of the fault-plane traction-vector components, and T_v^0 is the corresponding initial equilibrium value. The slip and slip-velocity vectors are then

$$\begin{aligned} s_v(t) &= u_v^+(t) - u_v^-(t) \\ \dot{s}_v(t + \Delta t/2) &= \dot{u}_v^+(t + \Delta t/2) - \dot{u}_v^-(t + \Delta t/2). \end{aligned} \tag{4}$$

To find the slip and slip velocity, we need to evaluate T_v. We define $\tilde{T}_v$ as the traction vector that would be required to enforce continuity of tangential velocity ($\dot{u}_v^+ - \dot{u}_v^- = 0$ for v equal to x and y) in (3). The expression for $\tilde{T}_v$, from D05, is

$$\tilde{T}_v \equiv \frac{\Delta t^{-1} M^+ M^- (\dot{u}_v^+ - \dot{u}_v^-) + M^- R_v^+ - M^+ R_v^-}{a (M^+ + M^-)} + T_v^0, \; v = x, y, \tag{5}$$

where the velocities are evaluated at $t - \Delta t/2$, and the nodal tractions, restoring forces, and displacements are evaluated at t. The fault-jump conditions (1) and (2) are satisfied (D05) if the fault-plane traction T_v of equation (3) is

$$T_v = \begin{cases} \tilde{T}_v & \text{for } [(\tilde{T}_x)^2 + (\tilde{T}_y)^2]^{1/2} \le \tau_c \\ \tau_c \dfrac{\tilde{T}_v}{[(\tilde{T}_x)^2 + (\tilde{T}_y)^2]^{1/2}} & \text{for } [(\tilde{T}_x)^2 + (\tilde{T}_y)^2]^{1/2} > \tau_c, \end{cases} \tag{6}$$

for $v = x, y$.

SG Fault Formulation

We adapt the SG method of Andrews (1976a, 1999) to the fourth-order VSSG FD code of Pitarka (1999). Pitarka's code permits variable-size grid spacing, but our implementation is restricted to the special case of constant grid spacing (in which case the spatial differencing retains fourth-order accuracy). In this FD method, the respective components of velocity and stress are calculated at different discrete points, as shown in Figure 2. Detailed descriptions of this FD method are given in several references (e.g., Graves, 1996; Pitarka, 1999).

The principal difference between the TSN method and the SG formulation is that the latter does not place velocity nodes on the fault, but instead positions the fault to coincide with the standard grid points already containing the fault-plane traction components. The fault discontinuity is represented through inelastic increments to those traction components. The nearest velocity nodes are offset by a distance $\Delta x/2$ to either side of the fault, where Δx is the dimension of the unit cell (equal in all three coordinate directions) of the grid, making the fault in this formulation indistinguishable from an inelastic zone of thickness Δx, as shown in Figure 2.

We again take the $x - y$ plane as the fault surface. In the split-node method, we introduced extra grid variables T_x and T_y on the fault to represent the traction-vector components at the split nodes. In the SG method, no extra tractions have to be introduced to accommodate the fault; the fault-plane traction components are located at the standard grid points for the tensor components σ_{xz} and σ_{yz}, respectively. However, we continue to use T_x and T_y to denote these two shear-traction components when they are located on the fault, for notational consistency with the split-node discussion.

Because of the way stresses are staggered in the VSSG method, T_x and T_y are located at different sets of fault-plane points, so interpolation would be required to evaluate the full traction vector at a common point. As a simplification, we specialize to the case where the shear prestress is in the x direction, that is, $T_y^0 = 0$, and further assume that, during sliding, friction always acts in the prestress direction. This neglect of the effect of rake rotation on friction direction is unimportant in the problem considered here, in which rake direction varies little.

The standard VSSG method updates nodal stresses by central differencing in time by using strain rates calculated from nodal velocities at $t - \Delta t/2$. For example, for the shear stress component σ_{xz} at a particular point, this takes the form

$$\sigma_{xz}(t) = \sigma_{xz}(t - \Delta t) + \Delta t 2\mu\dot{\varepsilon}_{xz}\,(t - \Delta t/2), \tag{7}$$

where $\dot{\varepsilon}_{xz}\,(t - \Delta t/2)$ is the strain rate and μ is the shear modulus. To implement the SG method, we modify this stress update scheme when calculating fault-plane traction components $T_x(t)$ by the addition of an inelastic component to the total strain rate:

$$T_x(t) = T_x(t - \Delta t) + \Delta t 2\mu[\dot{\varepsilon}_{xz}\,(t - \Delta t/2) - \dot{\varepsilon}^p_{xz}\,(t - \Delta t/2)]. \tag{8}$$

Then we calculate a trial value, $\tilde{T}_x(t)$, where $\tilde{T}_x(t)$ is just $T_x(t)$ as it would be computed in the unmodified VSSG method, that is, provisionally setting $\dot{\varepsilon}^p_{xz}\,(t - \Delta t/2)$ to zero:

$$\tilde{T}_x(t) = T_x(t - \Delta t) + \Delta t 2\,\mu\dot{\varepsilon}_{xz}\,(t - \Delta t/2). \tag{9}$$

We then set the fault-plane traction to

$$T_x(t) = \begin{cases} \tilde{T}_x(t) & \text{if } \tilde{T}_x(t) \le \tau_c \\ \tau_c & \text{if } \tilde{T}_x(t) > \tau_c \end{cases} \tag{10}$$

to satisfy (with the simplification mentioned previously) condition (1). Inserting (10) into (8) and using (9) to eliminate $T_x(t - \Delta t)$, we solve for $\dot{\varepsilon}^p_{xz}$:

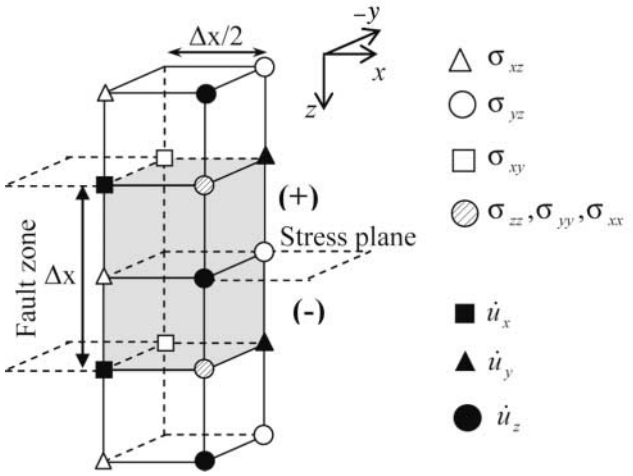

Figure 2. Stress glut inelastic-zone model implemented in a VSSG FD formulation. The fault-jump conditions are approximated by modifying the shear-stress components located along a plane coinciding with the fault (labeled "stress plane"). This is equivalent to an inelastic zone of one grid-step (Δx) thickness.

$$\dot{\varepsilon}^{p}_{xz}(t - \Delta t/2) = \frac{\tilde{T}_x(t) - T_x(t)}{2\mu\Delta t}. \quad (11)$$

Finally, we calculate the total slip rate on the fault by integrating the inelastic strain rate over the spatial step Δx in the direction normal to the fault, which gives

$$\dot{s}_x(t - \Delta t/2) = 2\Delta x\dot{\varepsilon}^{p}_{xz}\ (t - \Delta t/2), \quad (12)$$

from which the slip is then updated by central differencing,

$$s_x(t) = s_x(t - \Delta t) + \Delta t\dot{s}\ (t - \Delta t/2)\ . \quad (13)$$

TF Formulation

The TF formulation proposed by Madariaga *et al.* (1998) is similar to the SG method and was also designed to work with the VSSG FD scheme. As in the SG formulation, no explicit fault discontinuity is introduced at the velocity nodes. Instead, also as in the SG method, the shear-stress conditions are set at standard stress grid points of the staggered grid.

The TF method differs from SG in three respects, however.

1. Instead of placing the fault to coincide with a plane of shear-stress grid points, it is placed halfway between two planes of shear-stress grid points, as shown in Figure 3 (again taking the $x - y$ plane as the fault surface).
2. The stress conditions given by equations (1) and (2) (together with the friction law) are set in two adjacent stress planes one grid step Δx apart, stress planes $(+)$ and $(-)$ (see Fig. 3), instead of in a single stress plane as in the SG method. Thus, TF approximation of the jump conditions (1) and (2) entails an inelastic fault zone of two-grid-steps thickness in the fault-normal (z) direction; for given fault-plane coordinates (x,y), the shear stresses on these two planes are equal during sliding. This characteristic of the TF method apparently restricts it to symmetric fault problems.
3. A trial traction is calculated by (9), and modified by (10), as in SG, but the slip velocity is not calculated from an equivalent inelastic strain (equations 8 and 11–13). Instead, the slip velocity is defined as the velocity at nodes on opposite edges of the inelastic zone, that is, on velocity planes $(+)$ and $(-)$ in Figure 3, which are $2\Delta x$ apart:

$$\dot{s}_x\ (t - \Delta t/2) = \dot{u}_x^{(+)}\ (t - \Delta t/2) - \dot{u}_x^{(-)}(t - \Delta t/2), \quad (14)$$

where $\dot{u}_x^{(+)}$ and $\dot{u}_x^{(-)}$ are particle velocities at the $(+)$ and $(-)$ planes (not to be confused with the split-node velocities $\dot{u}_v^{\pm}$ from the TSN method). A part of this velocity difference is due to the elastic part of the inelastic-zone response, so, unlike the SG method, the TF method fails to preserve this distinction in estimating slip velocity. As a final step, slip is obtained from (13), that is, via the central differencing formula.

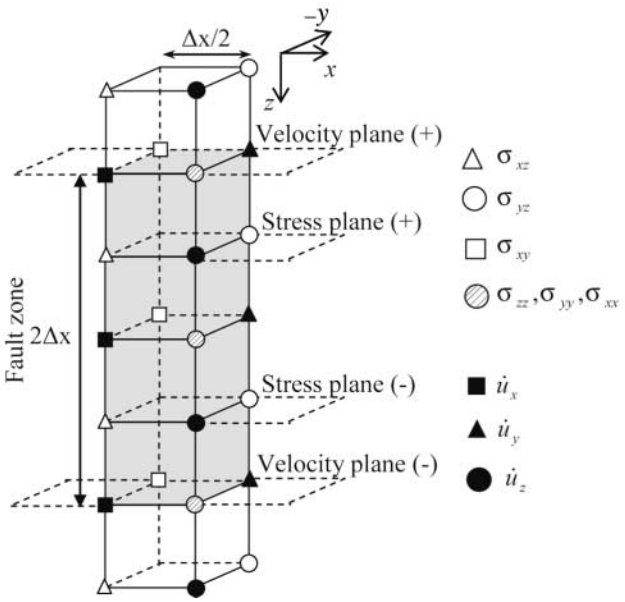

Figure 3. Thick fault inelastic-zone model implemented in a VSSG FD formulation (Madariaga *et al.*, 1998). The fault-jump conditions are approximated by modifying the shear-stress components located along a pair of parallel planes equidistant from the fault (labeled "stress plane"). This is equivalent to an inelastic zone of two grid steps ($2\Delta x$) thickness.

Numerical Test

To assess the SG and TF methods, we solve the 3D spontaneous-rupture benchmark problem proposed by Harris *et al.* (2004) for a planar fault embedded in a uniform elastic isotropic space. This test was selected because D05 solved this problem numerically by two different methods, the BI method and the so-called DFM implementation of the TSN method (Day, 1982a,b; Day and Ely, 2002). They examined numerical results for a range of Δx values and found that the BI and DFM computations converged to a common solution, within well-defined tolerances that they interpreted as approximate error bounds on the solution. We will use the highest-resolution solution available in D05, which is denoted solution DFM0.05, as the reference for evaluation of all SG and TF solutions.

The formulation and parameters of the test case correspond to Version 3 of the Southern California Earthquake Center (SCEC) benchmark problem (Harris *et al.*, 2004). The problem geometry is shown in Figure 4. We take the fault plane to be the $x - y$ plane. The shear prestress is aligned with the x axis, and the origin of the coordinate system is located in the middle of the fault, as shown in Figure 4. The

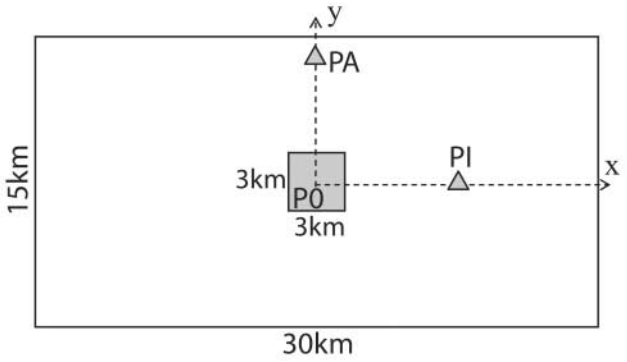

Figure 4. Fault model (from Harris *et al.*, 2004) for testing dynamic rupture simulations. The square in the center is the nucleation area. The triangles are the receivers at which we compare time histories of slip, slip rate, and shear stress. Relative to an origin at the center of the fault, the receiver P0, located in the hypocenter, has *y* coordinate 0, and *x* coordinate 0, PI has *y* coordinate 0, and *x* coordinate 7.5, and the receiver PA has *x* coordinate 0, and *y* coordinate 6.0 km. The stress parameters are specified in Table 1.

fault and prestress geometries are such that the *x* and *y* axes are axes of symmetry (or antisymmetry) for the fault-slip and traction components. As a result, the *xz* plane undergoes purely in-plane motion, and the *yz* plane purely antiplane motion.

Rupture is allowed within a fault area 30 km in the *x* direction and 15 km in the *y* direction. A homogeneous medium is assumed, with a *P*-wave velocity of 6000 m/sec, *S*-wave velocity of 3464 m/sec, and density of 2670 kg/m^3. The distributions of the initial stresses and frictional parameters on the fault are specified in Table 1. The nucleation occurs in 3 km $\times$ 3 km square area that is centered on the fault, as shown in Figure 4. The rupture initiates because the initial shear stress in the nucleation patch is set to be slightly (0.44%) higher than the initial static yield stress in that patch. Then the rupture propagates spontaneously through the fault area, with the frictional strength τ_c proportional to normal stress σ_n (taken negative in compression):

$$\tau_c = -\mu_f(\ell)\sigma_n. \tag{15}$$

The coefficient of friction $\mu_f(\ell)$ depends on the slip path length, $\ell = \int_0^t \dot{s}(t')dt'$, through the linear slip-weakening relationship,

$$\mu_f = \begin{cases} \mu_s - (\mu_s - \mu_d)\ell/d_0 & \ell < d_0 \\ \mu_d & \ell \geq d_0 \end{cases}, \tag{16}$$

where μ_s and μ_d are coefficients of static and dynamic friction, respectively, and d_0 is the critical slip-weakening distance (e.g., Ida, 1972; Andrews, 1976a,b; Day, 1982b; Madariaga *et al.*, 1998; Dalguer *et al.*, 2001). The rupture cannot propagate beyond the specified 30 km $\times$ 15 km region because of the high static frictional strength set outside the region.

First, we compute two relatively fine-mesh solutions, with grid intervals $\Delta x = 0.05$ km and 0.1 km, respectively, for each of the three methods: DFM, SG, and TF. At this stage, we focus on quantitative and qualitative comparisons of the solutions obtained with a common grid size interval Δx. We name the solutions using the same convention used in D05: the calculations for $\Delta x = 0.05$ km, for example, are denoted by DFM0.05, SG0.05, and TF0.05, respectively, for the DFM, SG, and TF methods; and DFM0.1 denotes the DFM calculation with $\Delta x = 0.1$ km, with similar naming for the other cases. The quantitative comparison of solutions is made principally by means of the three global solution metrics proposed by D05. These are (1) root mean square average over the fault plane of the rupture time differences between solutions, where rupture time is defined as the time at which slip velocity first exceeds 1 mm/sec; (2) root-mean-square average, over the *x* and *y* axes, of the differences in final slip between solutions; and (3) root-mean-square average over the *x* and *y* axes of the differences in peak value of slip velocity.

Second, we compute a series of solutions with each method, using Δx up to 0.3 km to establish the degree to which grid-size invariance has been achieved in the numerical solutions. To quantify grid-size dependence, we employ the same three metrics described previously. Grid intervals and timesteps for all the solutions are shown in Table 2.

The cohesive zone is the portion of the fault plane behind the crack tip where the shear stress decreases from its static value to its dynamic value and slip path length ℓ satisfies $0 < \ell < d_0$ (e.g., Ida, 1972). In the cohesive zone, shear stress and slip rate vary significantly, and proper numerical resolution of those changes is crucial for capturing the maximum slip rates and the rupture-propagation speeds. We express the grid-size dependence of the solution in terms of the dimensionless ratio N_c introduced by D05, where N_c is the ratio of the width of the cohesive zone, Λ, to the grid interval Δx,

$$N_c = \Lambda/\Delta x. \tag{17}$$

This ratio provides a nondimensional characterization of the resolution of a given numerical solution. As discussed at length in D05, N_c is a local measure of resolution, because Λ varies as the rupture propagates. We would like to relate the solution accuracies, as assessed from our three global metrics, to some global measure of the degree of resolution of the cohesive zone. To characterize the latter, we use the average number of spatial elements (grid points) within the cohesive zone, as given by the median value $\overline{N}_c$ of the local resolution number N_c, where the median is taken over the *x* axis (see D05 for a discussion of the spatial variability of N_c and the relationship between $\overline{N}_c$ and other global measures of resolution). We begin with the cohesive zone width Λ calculated in D05 from the reference solution DFM0.05, and

Table 1
Dynamic Stress Parameters for Spontaneous Dynamic Rupture Simulation

Parameters	Within Fault Area of 30 km × 15 km		Outside Fault Area
	Nucleation	Outside Nucleation	
Initial shear stress (MPa) (τ_0)	81.6	70.0	70.0
Initial normal stress (MPa) ($-\sigma_n$)	120.0	120.0	120.0
Static friction coefficient (μ_s)	0.677	0.677	infinite
Dynamic friction coefficient (μ_d)	0.525	0.525	0.525
Static yielding stress (MPa) ($\tau_{cs} = -\mu_s * \sigma_n$)	81.24	81.24	infinite
Dynamic yielding stress (MPa) ($\tau_{cd} = -\mu_d * \sigma_n$)	63.0	63.0	63.0
Dynamic stress drop (MPa) ($\Delta\tau = \tau_0 - \tau_{cd}$)	18.6	7.0	7.0
Strength excess (MPa) ($\tau_{cs} - \tau_0$)	−0.36	11.24	infinite
Critical slip distance (m) d_0	0.40	0.40	0.40

Table 2
Test Problem Calculations

Calculation Name	Solution Method	Spatial Step Δx (km)	Time Step Δt (sec)	Median Resolution $\bar{N}_c$
SG0.05/ TF0.05	SG/TF	0.05	0.0033	8.8
SG0.1/TF0.1	SG/TF	0.1	0.0066	4.4
SG0.15/ TF0.15	SG/TF	0.15	0.0099	2.9
SG0.2/TF0.2	SG/TF	0.2	0.013	2.2
SG.25/TF0.25	SG/TF	0.25	0.016	1.8
SG0.3/TF0.3	SG/TF	0.3	0.02	1.5
DFM0.05	DFM	0.05	0.005	8.8
DFM0.075	DFM	0.075	0.00625	5.9
DFM0.1	DFM	0.1	0.008	4.4
DFM0.15	DFM	0.15	0.0125	2.9
DFM0.2	DFM	0.2	0.016	2.2
DFM0.25	DFM	0.25	0.015	1.8
DFM0.3	DFM	0.3	0.020	1.5

calculate its median value, $\bar{\Lambda}$, which is 0.44 km. Then, for any solution with grid spacing Δx, we define $\bar{N}_c$ to be

$$\bar{N}_c = \bar{\Lambda}/\Delta x \tag{18}$$

(always using the DFM0.05 value of 0.44 km for $\bar{\Lambda}$). Table 2 lists the median-resolution value $\bar{N}_c$ for each calculation. An alternative measure would be $N_c^{\min}$, the minimum value of N_c. As noted in D05, $N_c^{\min}$ for this test problem is roughly ¾ $\bar{N}_c$.

Comparisons of Fine-Mesh Solutions

We assess the two highest-resolution solutions (the Δx 0.05 km and 0.1 km cases), as obtained, respectively, with the SG and TF methods (SG0.05, SG0.1, TF0.05, and TF0.1), by comparing them with reference solution DFM0.05. To reduce clutter in the plots, we usually will not show comparisons with DFM0.1, because it is nearly identical with DFM0.05, and extensive comparisons between the two DFM solutions have already been documented in D05.

For consistency with previous work (e.g., Madariaga *et al.*, 1998), the two fault-zone models (SG and TF) were initially implemented in a fourth-order staggered-grid code, such that the fourth-order spatial-difference operators were used even along the fault zone (Figs. 2 and 3) where some of the field variables are discontinuous. With this formulation, the TF0.1 fault-zone model is not able to break the fault and propagate beyond the overstressed nucleation zone. This remained the case for grid intervals Δx down to the smallest value that was computationally tractable for us in this study (0.05 km). Therefore, we modified the TF method slightly from its published form by replacing the fourth-order spatial-difference operators by their second-order counterparts wherever the difference template crosses the fault. We use this modified TF method for all the subsequent TF simulations. With this partially second-order formulation, the TF0.05 and TF0.1 models break out of the nucleation zone and propagate over the fault surface, but all TF models with Δx greater than 0.1 km still fail to do so. We also tested a similar partially second-order modification of the SG method, but the modified SG results are indistinguishable from those of the fully fourth-order SG implementation, and we only present results for the latter. The SG method gives a propagating rupture solution for all values of Δx considered in this study (up to 0.3 km), as does the DFM method.

We first compare the rupture front propagation and cohesive zone development for the SG and TF solutions with the reference solution DFM0.05. Figure 5 shows the cohesive zone as it develops along both x (inplane) and y (antiplane) axes, for SG0.05, SG0.1 and the reference solution. Figure 6 shows the corresponding results for the TF method, and Figure 7 plots cohesive zone widths (top) and rupture velocities (bottom) for each case. As shown in Figure 5, the SG solutions produce a rupture with a cohesive-zone width that varies with propagation distance in a manner similar to that of the reference solution, but it is systematically narrower. This effect is shown again at the top of Figure 7. Although the cohesive-zone-width curves for both SG solutions have roughly the same shape as those of the reference solution, the SG widths are systematically lower. Along the in-plane (x) axis, for example, the width discrepancy relative to the

reference solution is about 25% for SG0.1 and somewhat less for SG0.05. But along the antiplane (y) axis this discrepancy reduces to about 15% for SG0.1 and to less than 2% for SG0.05. Figure 5, and the bottom frame of Figure 7, show that the rupture velocity in the SG solutions is systematically slower than the reference solution in both principal directions. The error along the in-plane axis is about 4% for SG0.1 and about 1.5% for SG0.05. For comparison, Figure 7 also shows the split-node solution for $\Delta x = 0.1$ km DFM0.1. Relative to reference solution DFM0.05, the rupture-velocity errors of SG0.05 are slightly greater than the rupture-velocity errors of DFM0.1. Likewise, the cohesive-zone width errors of SG0.05 are larger than those of DFM0.1. In other words, to achieve a given accuracy in the time (or velocity) of rupture, the cohesive-zone resolution requirement N_c is more than twice as large for SG as for the split-node DFM scheme. Later we will further quantify this difference in resolution requirement.

The TF errors for cohesive-zone width and rupture time are far greater than those for the other methods, as shown in Figures 6 and 7. Errors in cohesive zone width are 30 to 70% for TF 0.1, and only slightly lower for TF0.05. The TF rupture velocities are anomalously low, with rupture times that are too late by as much as 100% in some cases (e.g., near the end of the antiplane axis) for TF0.1, and exceed 25% even for TF0.05. Rupture velocities in both TF solutions drop spuriously, and for a prolonged period, shortly after the breakout from the nucleation patch, with the TF0.1 rupture almost stopping after propagating 4 to 5 km. Thus, it is difficult to see how either TF solution would be useful even for providing qualitative understanding of the test problem.

The more stringent (relative to DFM) gridding requirement for modeling rupture velocities accurately with SG is probably a consequence of the blunting of the stress concentration on the rupture, a consequence of the SG fault condition being indistinguishable from an inelastic zone of thickness Δx. This is evident in Figure 8, which shows shear-stress time histories at fault points P0 (the hypocenter) and PI (along the x axis—see Fig. 4) for SG, TF, and reference (DFM0.05) solutions. At PI, the SG stress histories follow the shape of the reference solution and match the timing of the small initial peak and subsequent trough (at about 2.5 sec), but then rise more slowly to the maximum, slightly delaying the onset of rupture. The TF solutions poorly resolve the initial rise and fall of stress and then greatly delay the onset of peak stress. In addition, the stress drop at the rupture front is appreciably slower in the TF solutions than in the others. The much poorer stress resolution of TF is attributable in part to additional crack blunting due to the $2\ \Delta x$ thickness (i.e., twice that for SG) of the equivalent inelastic zone that represents the fault, but this may not entirely account for the large error. A second factor that may contribute is the failure of the TF method to separate elastic and inelastic components of the displacement jump across the fault zone, although it is unclear precisely how that feature would operate to delay rupture.

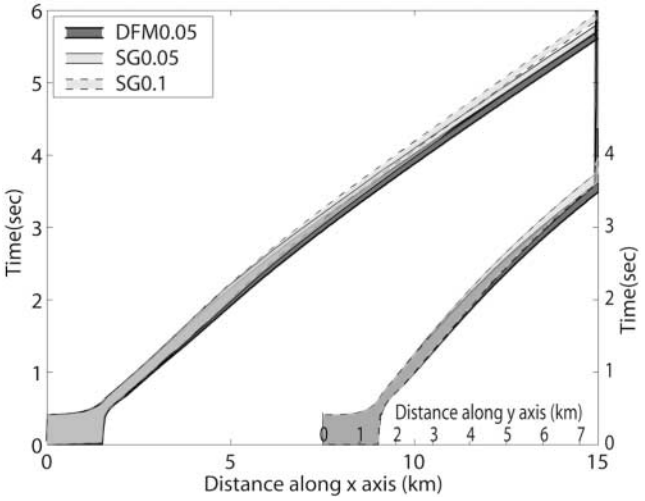

Figure 5. Cohesive-zone development, in both in-plane (x) and antiplane (y) directions, for SG0.05, SG0.1, and reference (DFM0.05) solutions. Notice that that there is some overlap of cohesive zones from different methods, so that the full width for DFM is not clearly shown.

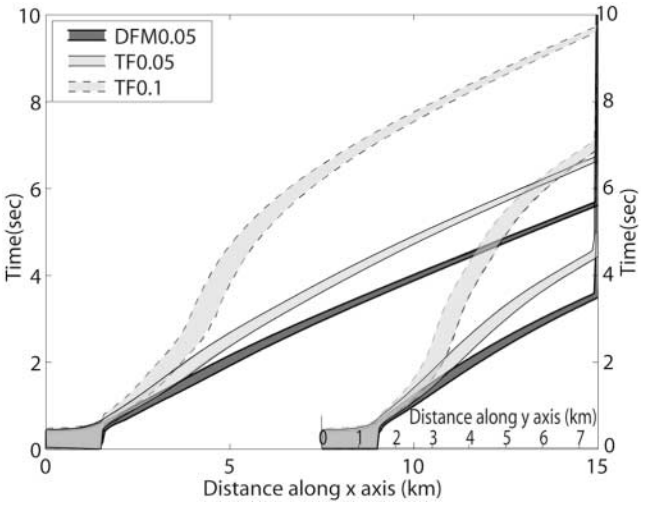

Figure 6. Cohesive-zone development, in both antiplane (y) and in-plane (x) directions, for TF0.05, and TF0.1, and reference (DFM0.05) solutions.

Figure 9 shows contours of rupture time for the reference solution (DFM0.05), as well as for the DFM0.1, SG0.1, and SG0.05 solutions (TF solutions are not included). Note that, for consistency with Harris *et al.* (2004) and D05, the rupture time is defined here as the time at which the slip rate of a point on the interface first exceeds 1.0 mm/sec (although results obtained with rupture time defined as the time when the shear stress first reaches the static friction value are nearly the same as those obtained with the 1.0 mm/sec criterion). The computed evolution of the rupture time is virtually identical for the DFM0.05 and DFM0.1 solutions, so that the contours for these two cases overlay and are nearly

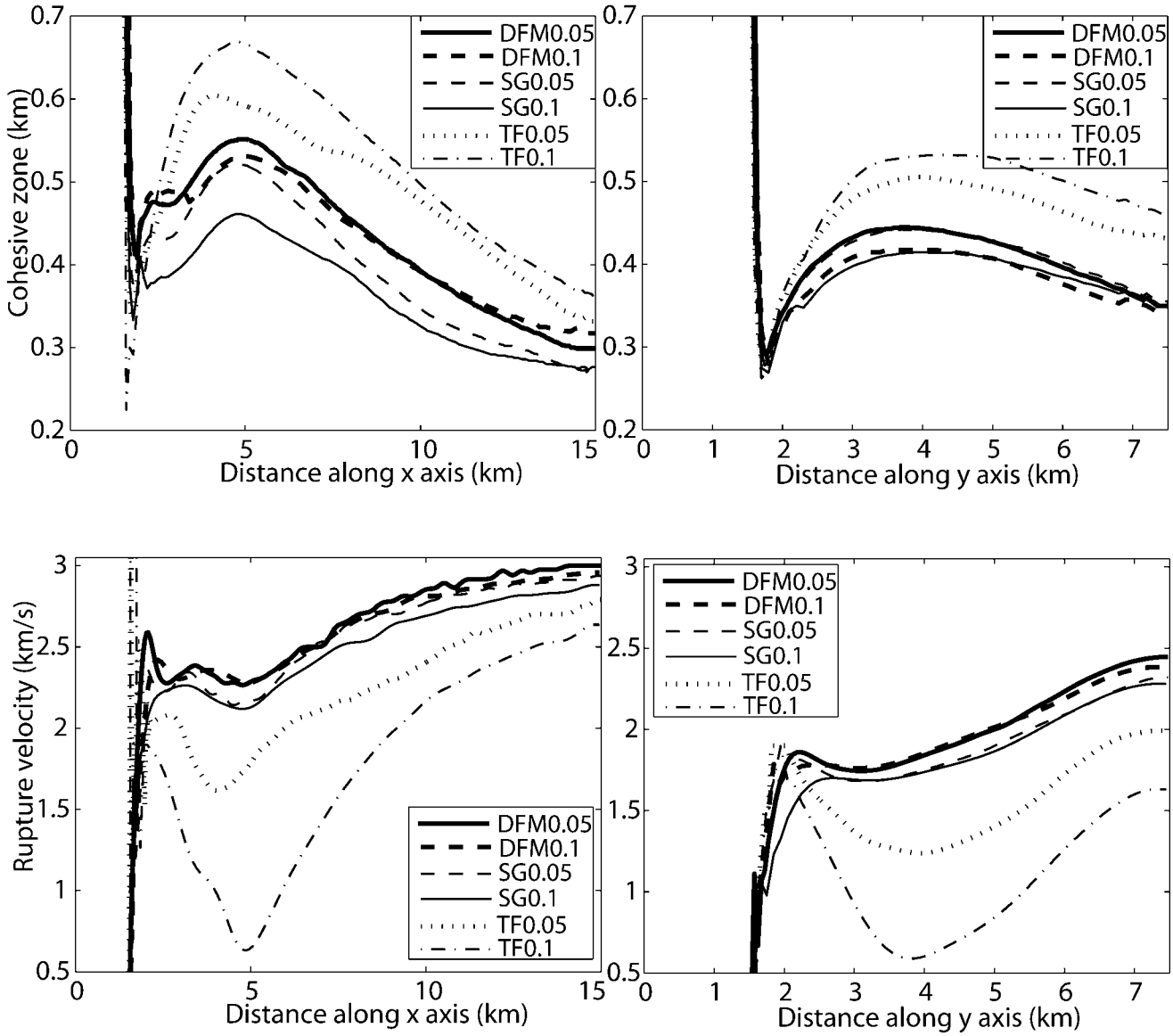

Figure 7. Cohesive zone size (top) and rupture velocity (bottom) along the in-plane (x) and anti-plane (y) directions, for DFM0.05, DFM0.1, SG0.05, SG0.1, TF0.05, and TF0.1 solutions.

indistinguishable in Figure 9. The systematic lag of the two SG solutions is clear in the figure. The SG and DFM models have rupture contours that are very close together right after the initiation of the rupture, with larger differences in the rupture time arising later. Thus, rupture-time differences between SG and DFM cannot be accounted for by a simple time delay due to differences in nucleation, but represent systematic differences in rupture velocity over the entire rupture. This can also be seen in the rupture velocity versus distance plots in Figure 7, where it is clear that the SG solutions, even the highest-resolution one, have rupture velocity that is biased low almost everywhere on the fault. Relative to the reference solution, the maximum misfit in rupture time of SG0.05 is 0.13 sec (3.6%), and the root-mean-square (rms) misfit is 0.09 sec (2.5%) (as in D05, an rms averaging of the rupture arrival-time difference is taken over the entire fault plane). The maximum and rms misfits of SG0.1 are 0.29 sec (8.1%) and 0.18 sec (5%), respectively. For comparison, DFM0.1 has rms rupture-time misfit of 0.011 sec (0.31% of the mean rupture time) and maximum misfit of 0.046 sec (1.3% of mean rupture time). These small rupture-time misfits between DFM0.05 and DFM0.1 are comparable to our uncertainty in the absolute accuracy of DFM0.05 itself, if we estimate that uncertainty from the difference between DFM0.05 and a boundary integral solution reported by D05. The DFM0.05 and boundary integral solutions in D05 have 1.3% maximum, and 0.8% rms time differences, which can serve as rough measures of that uncertainty. So SG0.05 and

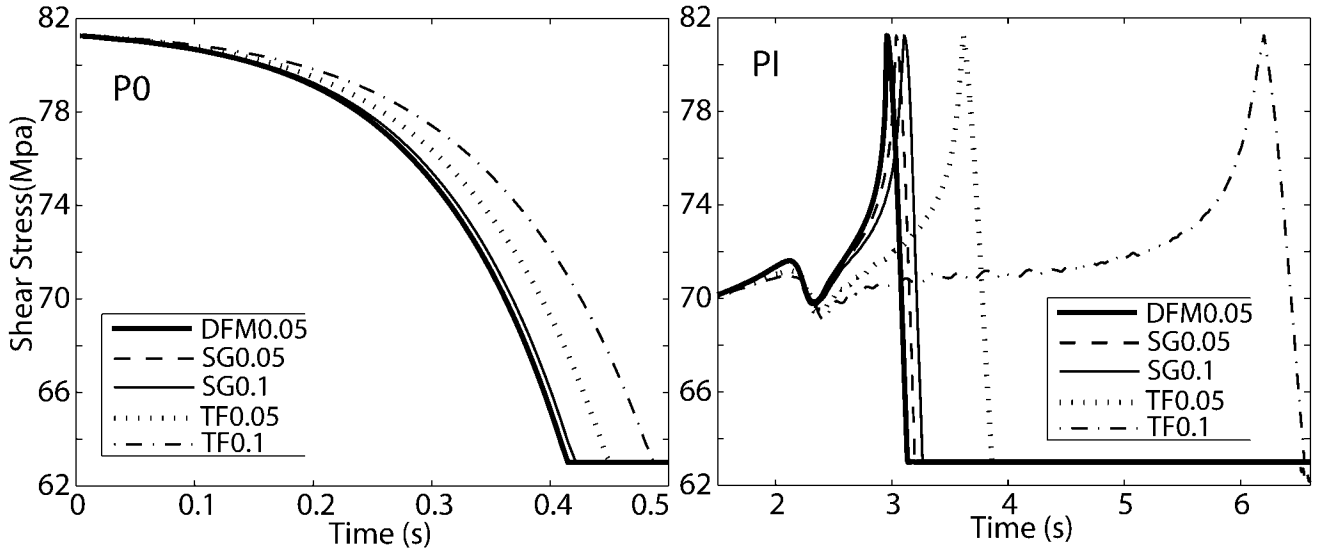

Figure 8. Time history of the shear-stress function at the hypocenter (P0) and at point PI (see Fig. 4), for DFM0.05, SG0.05, SG0.1, TF0.05, and TF0.1 solutions.

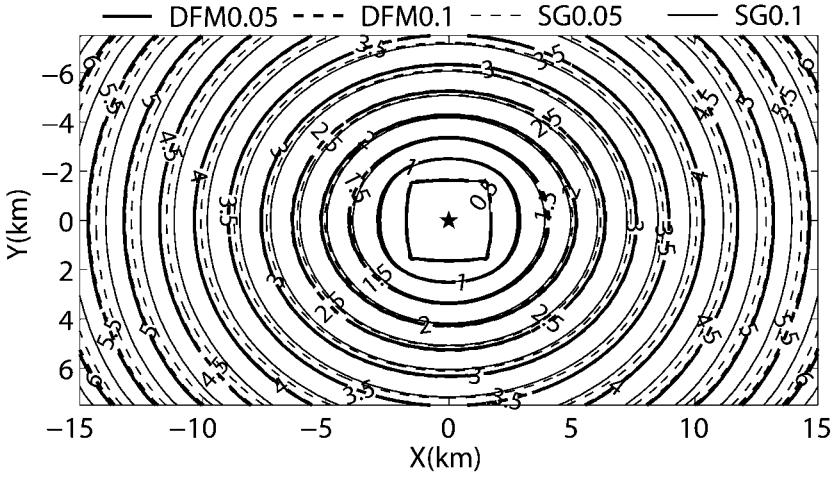

Figure 9. Contour plot of the rupture front for the test problem. Results are shown for DFM0.05, DFM0.1, SG0.05, and SG0.1 solutions.

SG0.1 have rms misfits roughly three and six times greater, respectively, than our estimated uncertainty in the reference solution itself. Tables 3 and 4 summarize the rms and maximum errors, respectively, for all the solutions.

Figure 10 shows the time histories of shear stress, slip, and slip velocity, at the two fault-plane points marked in Figure 4, one each on the in-plane (point PI) and antiplane (point PA) axes, respectively. For slip and stress, we compare only SG0.1 with the reference solution DFM0.05. We do not show SG0.05 because the final slip and shear stress in that case were affected by the reflected waves coming from the artificial boundaries. The rupture front arrival and peak slip velocities were not affected, however, because they develop before the arrival of the artificial reflected waves. We were able to use a larger mesh for SG0.1, so this problem does not affect that solution. DFM is a parallelized code, so we were able to use a mesh big enough to avoid the effect of artificial boundaries for the DFM0.05 reference solution as well (a calculation requiring 17.8 GB of memory, as discussed in D05). However, we did not have available a suitable parallel code for the SG calculations. As shown in the upper part of Figure 10, the shear stress and slip for SG0.1 are nearly identical with the reference solution along the in-plane and antiplane directions, except for the shifting in the arrival time. However, there is a notable discrepancy in the oscillations of the slip rate shown in the bottom part of this same figure. SG0.1 shows, at the PI receiver, a high level of oscillation, with fluctuation amplitude of about 50% of the peak velocity. However, this oscillation is considerably reduced for the SG0.05 solution, to about 5% of peak velocity, as shown in the zoom at the onset of the slip velocity. In contrast, the oscillation in the PA receiver is only about 3% of the peak velocity. The oscillations reflect the stringent resolution requirement for SG, so that the SG0.1 solution is quite poorly resolved, relative to SG0.05, and especially compared with the DFM solutions. However, we do not

Table 3
RMS Difference of Rupture Time
(in % of the Average Rupture Time of 3.57 sec)

	Method			
Δx (km)	DFM	SG	TF (2nd order)	TF (4th order)
0.05	0.0	2.52	23.4	35.1
0.075	0.15	N/A	N/A	N/A
0.1	0.31	5.04	93.0	infinite
0.15	1.26	8.62	infinite	infinite
0.2	2.72	14.0	infinite	infinite
0.25	5.02	21.3	infinite	infinite
0.3	8.50	30.4	infinite	infinite

Table 4
Maximum Difference of Rupture Time
(in % of the Average Rupture Time of 3.57 sec)

	Method			
Δx (km)	DFM	SG	TF (2nd order)	TF (4th order)
0.05	0.0	3.4	32.6	48.0
0.075	0.50	N/A	N/A	N/A
0.1	1.30	8.2	115.0	infinite
0.15	3.57	14.42	infinite	infinite
0.2	6.41	22.82	infinite	infinite
0.25	10.1	33.76	infinite	infinite
0.3	15.55	46.9	infinite	infinite

know why the resulting oscillations are worse at point PI than at PA.

Grid Dependence

We continue to use the DFM0.05 solution as the reference, and quantify the misfits of the SG and TF solutions as functions of Δx, or equivalently, as functions of resolution number $\overline{N}_c$. For comparison, we also reproduce the results from D05 showing the scaling of DFM misfits with Δx. Our metrics are the same three introduced in D05: the rms rupture time metric discussed in the previous section, rms misfit of final slip, and rms misfit of peak slip rate. The rupture-time misfits are summarized in Figure 11 and the final slip and peak slip rate misfits in Figure 12. Note that the abscissa is denoted in two different ways in these figures: on the bottom, we show the grid spacing Δx; on the top, the corresponding cohesive-zone resolution number $\overline{N}_c$.

In Figure 11, the DFM, SG, and TF rupture-time misfits are denoted by solid circles, open circles, and open triangles, respectively. The dashed lines in this figure show the numerical timestep sizes as a function of Δx for the DFM, SG, and TF solutions. As noted by D05, the DFM solutions follow a remarkably well-defined power law in the grid size, with exponent, or convergence rate, of approximately 3. D05 also showed that both DFM and BI methods share a nearly identical convergence rate and that both achieve misfits comparable with (or less than) a single timestep for $\Delta x \leq 0.1$ km ($\overline{N}_c \leq \sim 4.4$).

In contrast, the SG misfits in Figure 11 do not show well-defined power-law convergence. The average slope obtained from linear regression gives an exponent of 1.4, which would suggest a convergence rate roughly half that of DFM (and BI). However, the slope is clearly not constant, and the misfit function appears to be leveling off to near-zero slope for small values of Δx. This behavior suggests that the SG0.05 misfit of 0.09 sec (2.5%) may become increasingly difficult to reduce through further grid-size reductions. It was not computationally feasible for us to examine this further, but, based on the available evidence it is quite uncertain whether SG is fully convergent to the reference solution (within our uncertainty estimates for the latter). Nonetheless, the rupture propagation behavior of the SG solution is qualitatively correct, and rupture time errors of less than 3% are attainable with $\overline{N}_c \sim 9$.

The rupture-time misfits for TF calculations, as shown in Figure 11, are available for two points only, TF0.05 and TF0.1, due to failure of solutions for Δx larger than 0.1 to propagate beyond the overstressed nucleation patch. As noted earlier (Fig. 6,7,8), the misfits are very high, the rms misfit reaching ~100% for TF0.1. The most we can say is that it is not computationally feasible to demonstrate convergence of the TF solution to this problem, nor to reduce the rms misfit to less than about 30%.

In Figure 12, diamonds are the rms misfits for the final-slip metric, and circles those for the peak slip-rate metric. Again, we show the DFM results from D05 (filled symbols) for reference, together with the SG results (open symbols). Because it is not computationally feasible to reduce the grid size much below 0.05 km, we do not analyze further the grid-size dependence of the TF solutions, and they are not included in Figure 12. For reference, however, the best resolved TF solution (TF0.05) has an rms misfit in final slip of about 5%, and in peak slip rate of about 26%. As was the case for the rupture times, the DFM method shows roughly power-law behavior for both metrics, although the scatter is somewhat greater for the peak slip-rate metric. For peak slip rate, DFM and SG have similar exponents of about 1.2, although, relative to DFM, SG requires $\overline{N}_c$ about three times as large (Δx reduced by a factor of ~3) to achieve comparable misfit reduction. For the final slip metric, the SG exponent (~0.7) is about half the DFM exponent (~1.5) (SG0.05 is omitted from the Fig. 12 final-slip results for the reason explained in the preceding section). The peak slip velocity misfit falls to ~10% or less for $\Delta x \leq 0.15$ km ($\overline{N}_c \geq 3$) for DFM and for $\Delta x \leq 0.05$ km ($\overline{N}_c \geq 9$) for SG. The final slip misfit falls to ~2% for $\Delta x \leq 0.15$ km ($\overline{N}_c > 3$) for DFM and for $\Delta x \leq 0.1$ km ($\overline{N}_c \geq 4.4$) for SG. Some caution is warranted in interpreting small differences in the final-slip metric for this test problem, given the abrupt termination of the slip at the edges of the fault. In problems of this type, final slip is expected to be proportional to the linear extent of rupture, and thus sensitive to differences of order Δx in effective

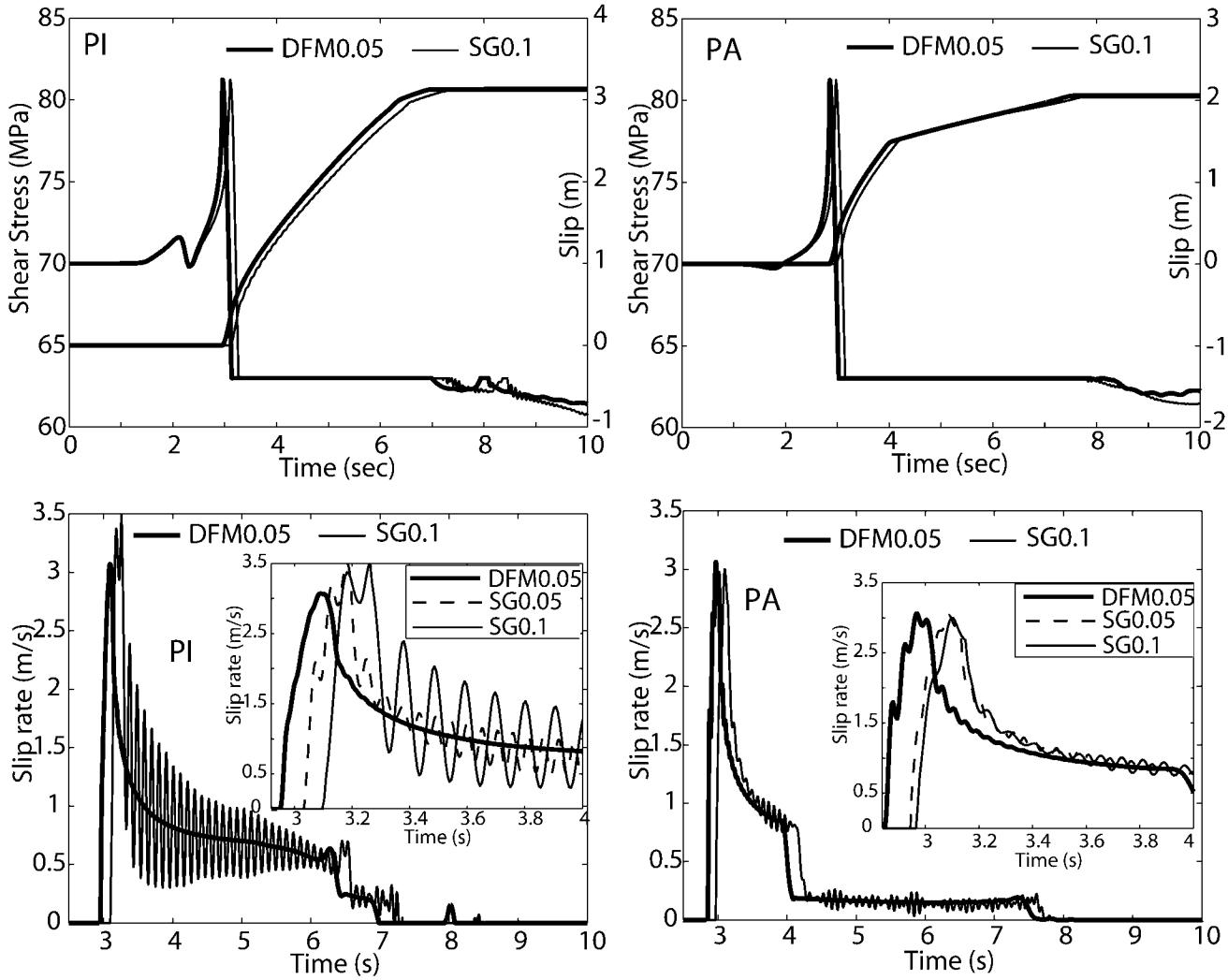

Figure 10. Time histories at the two fault-plane points marked in Figure 4. PI is on the in-plane (x) axis, and PA is on the antiplane (y) axis. Shear stress, slip, and slip velocity are shown, for solutions DFM0.05 and SG0.1. The zoom of slip rate, in the bottom, also shows SG0.05 solution.

rupture length that might arise between different numerical methods. On the other hand, note that the ~2% error of (for example) SG0.1 is several times larger than the corresponding percentage uncertainty in its effective fault length of ~0.1/15 (~0.7%).

Discussion and Conclusions

We provide quantitative assessments of the accuracy and grid-size dependence of two inelastic-zone fault representations that have been proposed for staggered-grid FD simulations of rupture dynamics, the TF method, and the SG method. The assessments are based on a well-validated reference solution obtained with a split-node FD method (DFM). Misfits relative to the reference solution are quantified using three metrics: rms differences in rupture time, final slip, and peak slip velocity, respectively.

The TF method in its original form, with fourth-order spatial differencing throughout the grid, achieves a propagating rupture only for the smallest computationally feasible Δx, corresponding to resolution number $\overline{N}_c \sim 9$ (i.e., with Δx small enough to resolve the cohesive zone with about nine grid points on average). When the original TF method is modified to reduce fault-crossing difference operators to second-order, a propagating solution is achieved for $\overline{N}_c =$ ~4.5 as well, but not for lower values of the resolution number (previously, Dalguer and Day [2004] also found, for a test problem specifically designed to facilitate propagating TF solutions, that TF consistently performed more poorly in its original form than with the previous modification). The TF solutions have quantitative misfits in rms rupture time of 30% and greater, and fail to match even the qualitative rupture behavior of the reference solution.

The SG method gives propagating rupture solutions for

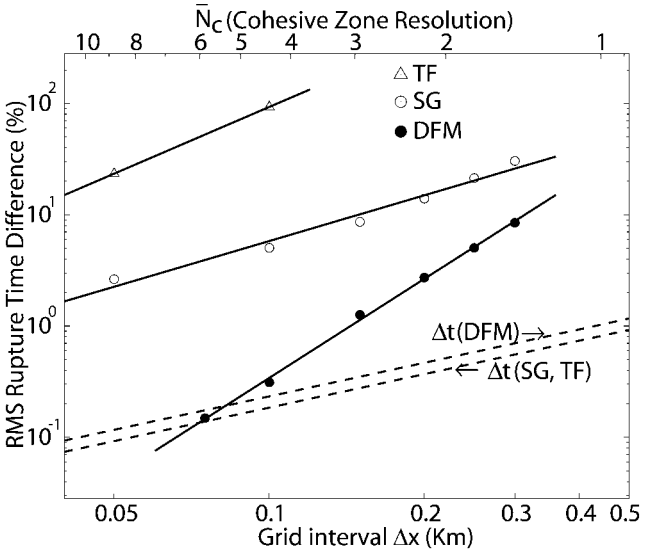

Figure 11. Misfits in time of rupture, relative to reference solution DFM0.05, shown as a function of grid interval Δx. Misfits are rms averages over the fault plane. Solid circles are DFM solutions, open circles are SG solutions, and triangles are TF solutions. The dashed lines show the (approximate) dependence of timestep Δt on Δx. The upper axis characterizes the calculations by their $\bar{N}_c$ values, where $\bar{N}_c$ is the median cohesive-zone width in the in-plane direction, divided by Δx. TF solutions are available only for TF0.05 and TF0.1, because for larger Δx TF does not give a propagating rupture solution to the test problem. SG does not appear to approach a well-defined power-law asymptote, as indicated by the concave-upward curvature of the misfit function, but the best-fitting exponent for SG over the available range of Δx is ~1.4. DFM solutions follow a power law with well-defined exponent of ~3 over this range (confidence intervals for the convergence rate are discussed in D05).

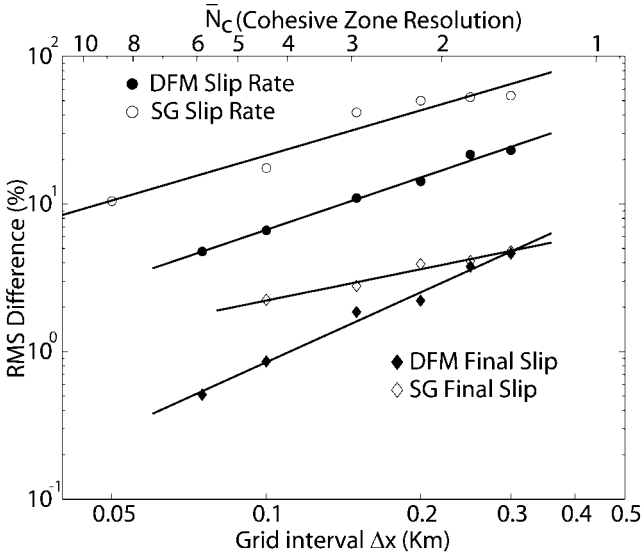

Figure 12. Misfits in final slip (diamonds) and peak slip velocity (circles), relative to reference DFM0.05 solution, shown as a function of grid interval Δx. Differences are rms averages over the x and y axes of the fault plane. Filled symbols are DFM solutions; open symbols are SG solutions. Note the power-law convergence of both methods as the grid size is reduced. As also observed for rupture time, the power-law exponent of final slip metric of DFM (1.52) is approximately twice that of SG (0.72). However, the exponent for the peak slip rate metric is approximately the same for both methods (~1.2).

all grid-interval values (Δx) considered here (0.05 to 0.3 km). For sufficiently small values of Δx, the method reproduces well the qualitative features of the reference solution. Results are nearly unchanged, whether the method is implemented with fourth-order spatial differencing everywhere, or with fault-crossing differences reduced to second-order. However, in either case, the SG method has significant quantitative deficiencies. Even at the smallest grid spacing considered, rupture velocity remains systematically low for SG relative to the reference solution. With respect to our rupture-time metric, SG lacks a well-defined power-law convergence, at least within the range of Δx that is currently computationally feasible. The rms rupture-time misfit for SG can be reduced to about 2.5% with $\bar{N}_c \sim 9$, but this misfit remains at least three times greater than the uncertainty in the reference solution. Furthermore, SG is relatively inefficient computationally, in the sense that this $\bar{N}_c$ requirement is about four times greater than that required for the split-node method to achieve comparable accuracy, and computation time scales as $(\bar{N}_c)^4$. The SG method does have simplicity of implementation in its favor, and may remain an attractive alternative for modeling faults with complex geometries. However, if SG were implemented with more than a single cell of inelastic-zone width (e.g., to capture geometrical complexities), its formulation would resemble that of the more poorly performing TF scheme. The DFM split-node method (detailed in D05) uses a type of computational grid that Moczo *et al.* (2006) have termed the "partly-staggered" grid. This differs in important respects from the VSSG method used in the TF and SG methods, and it might be thought that it is the grid type, rather than the fault-boundary representation, that results in the lower accuracy of TF and SG solutions relative to the split-node approach. However, Dalguer and Day (2006) have recently implemented a split-node scheme for the VSSG. They find that the resulting method is convergent, with a convergence rate nearly identical with that of the DFM method (which in turn was shown by D05 to be indistinguishable from the convergence rate of the boundary integral method).

Thus, we conclude that it is principally the numerical formulation of the jump conditions at the fault that controls solution accuracy in FD spontaneous-rupture simulations, and that neither grid type, nor order of spatial differencing in the grid interior, is of primary importance in that respect. Power-law convergence to a common solution has been

demonstrated for split-node FD and BI methods. In contrast, the TF inelastic-zone method does not achieve qualitatively meaningful solutions to the 3D test problem and is sufficiently computationally inefficient that it is not feasible to explore convergence. The SG inelastic-zone method achieves 3D test-problem solutions that are qualitatively meaningful and can be made quantitatively reliable to within a few percent. However, it remains uncertain whether the SG method is fully convergent, and it is in any event very computationally inefficient relative to the split-node approach.

Acknowledgments

We thank the two reviewers of this article, Joe Andrews and Peter Moczo, and the associate editor David D. Oglesby, for constructive comments and very helpful reviews that led to improvements in the manuscript. We are also very grateful to Arben Pitarka for providing us with his staggered-grid FD code. This work was supported National Science Foundation Grants ATM-0325033 and EAR-0122464 (SCEC Community Modeling Environment Project), and by SCEC. SCEC is funded by NSF Cooperative Agreement EAR-0106924 and U.S. Geological Survey Cooperative Agreement 02HQAG0008. The SCEC contribution number for this article is 956.

References

Aagaard, B. T, T. H. Heaton, and J. F. Hall (2001). Dynamic earthquake rupture in the presence of lithostatic normal stresses: Implications for friction models and heat production, *Bull. Seism. Soc. Am.* **91,** 1765–1796.

Andrews, D. J. (1973). A numerical study of tectonic stress release by underground explosions, *Bull. Seism. Soc. Am.* **63,** 1375–1391.

Andrews, D. J. (1976a). Rupture propagation with finite stress in antiplane strain, *J. Geophys. Res.* **81,** 3575–3582.

Andrews, D. J. (1976b). Rupture velocity of plane-strain shear cracks, *J. Geophys. Res.* **81,** 5679–5687.

Andrews, D. J. (1985). Dynamic plane-strain shear rupture with a slip-weakening friction law calculated by a boundary integral method, *Bull. Seism. Soc. Am.* **75,** 1–21.

Andrews, D. J. (1999). Test of two methods for faulting in finite-difference calculations, *Bull. Seism. Soc. Am.* **89,** 931–937.

Aochi, H., and E. Fukuyama (2002). Three-dimensional nonplanar simulation of the 1992 Landers earthquake, *J. Geophys. Res.* **107**, no. B2, 2035, doi 10.129/2000JB000061.

Cruz-Atienza, V. M., and J. Virieux (2004). Dynamic rupture simulation of non-planar faults with a finite-difference approach, *Geophys. J. Int.* **158,** 939–954.

Dalguer, L. A., and S. M. Day (2004). Split nodes and fault zone models for dynamic rupture simulation (abstract), *EOS Trans. AGU* **85,** no. 47, Fall Meet. Suppl., S41A-0944.

Dalguer, L. A., and S. M. Day (2006). Test of the split nodes fault model for faulting in staggered finite difference scheme (abstract of 2006 Annual meeting of the Seismological Society of America, 18–22 April 2006, San Francisco, California), *Seism. Res. Lett.* **77,** 219.

Dalguer, L. A., K. Irikura, and J. Riera (2003). Generation of new cracks accompanied by the dynamic shear rupture propagation of the 2000 Tottori (Japan) earthquake, *Bull. Seism. Soc. Am.* **93,** 2236–2252.

Dalguer, L. A., K. Irikura, J. Riera, and H. C. Chiu (2001). The importance of the dynamic source effects on strong ground motion during the 1999 Chi-Chi (Taiwan) earthquake: brief interpretation of the damage distribution on buildings, *Bull. Seism. Soc. Am.* **95,** 1112–1127.

Das, S. (1980). A numerical method for determination of source time functions for general three-dimensional rupture propagation, *Geophys. J. R. Astr. Soc.* **62,** 591–604.

Das, S., and K. Aki (1977). Fault planes with barriers: a versatile earthquake model, *J. Geophys. Res.* **82,** 5648–5670.

Das, S., and B. V. Kostrov (1988). An investigation of the complexity of the earthquake source time function using dynamic faulting models, *J. Geophys. Res.* **93,** 8035–8050.

Day, S. M. (1982a). Three-dimensional finite difference simulation of fault dynamics: rectangular faults with fixed rupture velocity, *Bull. Seism. Soc. Am.* **72,** 705–727.

Day, S. M. (1982b). Three-dimensional simulation of spontaneous rupture: the effect of nonuniform prestress, *Bull. Seism. Soc. Am.* **72,** 1881–1902.

Day, S. M., and G. P. Ely (2002). Effect of a shallow weak zone on fault rupture: Numerical simulation of scale-model experiments, *Bull Seism. Soc. Am.* **92,** 3006–3021.

Day, S. M., L. A. Dalguer, N. Lapusta, and Y. Liu (2005). Comparison of finite difference and boundary integral solutions to three-dimensional spontaneous rupture, *J. Geophys. Res.* **110,** B12307, doi 10.1029/2005JB003813.

Fukuyama, E., and R. Madariaga (1998). Rupture dynamic of a planar fault in a 3D elastic medium: rate- and slip-weakening friction, *Bull. Seism. Soc. Am.* **88,** 1–17.

Graves, R.W. (1996). Simulating seismic wave propagation in 3D elastic media using staggered-grid finite differences, *Bull Seism. Soc. Am.* **86,** 1091–1106.

Harris, R. A., R. Archuleta, B. Aagaard, J. P. Ampuero, D. J. Andrews, L. Dalguer, S. Day, E. Dunham, G. Ely, Y. Kase, N. Lapusta, Y. Liu, S. Ma, D. Oglesby, K. Olsen, and A. Pitarka (2004). The source physics of large earthquakes—validating spontaneous rupture methods (abstract), *EOS Trans. AGU* **85,** no. 47, Fall Meet. Suppl., S12A-05.

Ida, Y. (1972). Cohesive force across the tip of a longitudinal-shear crack and Griffith's specific surface energy, *J. Geophys. Res.* **77,** 3796–3805.

Inoue, T., and T. Miyatake (1998). 3D simulation of near-field strong ground motion based on dynamic modeling, *Bull. Seism. Soc. Am.* **88,** 1445–1456.

Kase, Y., and S. M. Day (2006). Rupture Processes on a bending fault, *Geophys. Res. Lett.* **33,** L10601, doi 10.1029/2006GL025865.

Lapusta, N., J. R. Rice, Y. Ben-Zion, and G. Zheng (2000). Elastodynamic analysis for slow tectonic loading with spontaneous rupture episodes on faults with rate- and state-dependent friction, *J. Geophys. Res.* **105,** 23,765–23,789.

Levander, A. R. (1988). Fourth-order finite-difference P-SV seismograms, *Geophysics* **53,** 1425–1436.

Madariaga, R. (1976). Dynamics of an expanding circular fault, *Bull. Seism. Soc. Am.* **66,** 639–666.

Madariaga, R., K. Olsen, and R. Archuleta (1998). Modeling dynamic rupture in a 3D earthquake fault model, *Bull. Seism. Soc. Am.* **88,** 1182–1197.

Moczo, P., J. Kristek, V. Vavryčuk, R. J. Archuleta, and L. Halada (2002). 3D heterogeneous staggered-grid finite-difference modeling of seismic motion with volume harmonic and arithmetic averaging of elastic moduli and densities, *Bull. Seism. Soc. Am.* **92,** 3042–3066.

Moczo, P., J. O. A. Robertsson, and L. Eisner (2006). The finite-difference time-domain method for modeling of seismic wave propagation, in *Advances in Wave Propagation in Heterogeneous Earth*, R-S. Wu and V. Maupin (Editors), in Advances in Geophysics series, **48,** Elsevier, doi 10.1016/S0065-2687(06)48008-0.

Mora, P., and D. Place (1994). Simulation of the Frictional stick-Slip Instability, *Pageoph* **143,** 61–87.

Morgan, J. K. (1999). Numerical simulation of granular shear zones using the distinct element method 2. Effects of particle size distribution and interparticle friction on mechanical mehavior, *J. Geophys. Res.* **104,** 2721–2732.

Oglesby, D. D., R. J. Archuleta, and S. B. Nielsen (1998). Earthquakes on

dipping faults: the effects of broken symmetry, *Science* **280,** 1055–1059.

Oglesby, D. D., R. J. Archuleta, and S. B. Nielsen (2000). The three-dimensional dynamics of dipping faults, *Bull. Seism. Soc. Am.* **90,** 616–628.

Olsen, K. B., R. Madariaga, and R. Archuleta (1997). Three dimensional dynamic simulation of the 1992 Landers earthquake, *Science* **278,** 834–838.

Pitarka, A. (1999). 3D elastic finite-difference modeling of seismic motion using staggered grid with nonuniform spacing, *Bull. Seism. Soc. Am.* **89,** 54–68.

Xia, K., A. J. Rosakis, H. Kanamori, and J. R. Rice (2005). Laboratory earthquake along inhomogeneous faults: directionality and supershear, *Science* **308,** 681–684, doi 10.1126/science.1108193.

Department of Geological Sciences
San Diego State University
San Diego, California 92182

Manuscript received 1 February 2006.